INTERNATIONAL JOURNAL of RENEWABLE ENERGY RESEARCH
Z. Massaq, Vol.13, No.1, March, 2023

Design of High–Performance Fuzzy–Predictive Controllers for a Photovoltaic/Battery Pumping System

Zakaria Massaq *‡

*Electrical Engineering Department, Faculty of Sciences and Technology, Beni Mellal, 23000, Morocco

(zakaria.massaq@gmail.com)

‡ Corresponding Author; Zakaria Massaq, Electrical Engineering Department, Faculty of Sciences and Technology,
Beni Mellal, 23000, Morocco.
Tel: +212– 523485112, zakaria.massaq@gmail.com

Received: 30.10.2022 Accepted: 05.12.2022

Abstract- In this paper, three cascaded fuzzy–predictive controllers are designed to control a photovoltaic/battery pumping system. For maximum power point tracking (MPPT), the outer loop consists of a fuzzy controller that provides the reference current corresponding to the maximum power. The inner loop regulates the photovoltaic current with a predictive controller based on pulse width modulation (PWM). Meanwhile, another fuzzy–predictive controller drives the bidirectional converter to manage the power flow between the different stages of the system. The third fuzzy–predictive controller consists of the duty ratio control (DRC) of the induction motor, in which a fuzzy estimator provides the switching vector (SV) to be applied to the inverter during the ON time (T_{ON}). Afterwards, a predictive controller calculates the optimal OFF time (T_{OFF}) for which a zero voltage will be applied. The proposed controllers are compared by simulation to three different control strategies presented in the literature. The system was subjected to different irradiances and speeds to test its performance under different environmental and load conditions. It turns out that the proposed MPPT algorithm provides the best tracking speed during system start-up and helps to reduce the PV power ripples. In addition, the battery current ripples are reduced, and the DC link voltage is regulated with zero overshoot and better accuracy. The proposed DRC is the best in terms of reducing torque and flux ripples and it tracks the reference speed with high accuracy. In addition, it can protect the motor from overcurrent.

Keywords Hybrid pumping system, Fuzzy–predictive control, Current ripples reduction, MPPT, Torque ripples reduction.

1. Introduction

Photovoltaic (PV) pumping technology is a great deal to the growth of advanced and developing economies. Photovoltaic water pumping systems (PVWPS)s are used in various applications such as agricultural irrigation, home use, industrial production, cleaning, and other applications [1]. A PVWPS may be categorized as a battery-less pumping system where the PV generator's power is fully converted into hydraulic power [2]. It can be classified into a pumping system based on a battery energy storage system (BESS), where the battery is connected to the DC–bus via a bidirectional DC-DC converter [3]. When the requirement arises, the BESS stores the excess energy. The stored energy can be used during the night or shading period to maintain the system operative all the time [4].

Most conventional maximum power point tracking (MPPT) algorithms are fixed step–size (SS) based. An adaptive SS improves the speed of power point tracking and minimizes high power fluctuations in steady–state. The conventional variable SS algorithm uses the term ($N.(|\Delta P_{pv}/\Delta V_{pv}|)$) as the incremented SS, where N is a constant multiplier, and $\Delta P_{pv}/\Delta V_{pv}$ is the derivative of photovoltaic power P_{pv} with respect to the photovoltaic voltage V_{pv} [5]. Nevertheless, a constant multiplier cannot guarantee the fast-tracking of the maximum power point (MPP) under enormous changes of insolation. In fact, the constant N is chosen only for particular irradiances. When the weather changes significantly, the tacking speed becomes slower. In [6], the conventional variable SS algorithm was replaced by an improved one, which uses an auto-scaling multiplier to achieve a better dynamic. The Fuzzy logic controller (FLC) has been used in various works for auto-tuning the SS [7, 8]. In the FLC, the design of membership functions (MF)s is made by human expertise [9], which gives more fluidity for choosing the optimal SS. For instance, in [10], an FLC generates a variable SS voltage perturbation (ΔV_{pv}) according to the absolute value of power slope $|\Delta P_{pv}/\Delta V_{pv}|$. In case of an abrupt change of irradiance, the current perturbation is preferred due to the proportional relationship between the PV current and incident sunlight [11]. For this reason, the current perturbation is employed in the present work.

Model predictive control (MPC) is an algorithm that uses the prediction model of the studied system to predict the next state of the variables to be controlled. The classical MPC for power converters calculates future tracking errors and builds a cost function with these errors. Afterwards, an iterative algorithm selects the best switching action that minimizes this function [12, 13]. However, the classical MPC algorithm does not ensure a fixed switching frequency operation. Variable switching frequency is not recommended for power converters because it makes the design of passive components difficult, increases the switching losses, and increases the total harmonic distortion [14, 15]. A predictive controller with a fixed switching frequency was suggested by [16] to control a boost converter's input voltage. The prediction model of the boost converter was employed for building a cost function and synthesizing the optimal duty ratio.

The use of the bidirectional DC-DC converter (BDC) between the battery and the DC bus is investigated in [17, 18]. The main advantage of the BDC is the voltage of the battery can be reduced, and it can realize the bidirectional power flow by functioning either as a buck or boost converter. Some recent papers [19, 20], have proposed the use of a proportional-integral (PI) controller to drive the BDC. Nevertheless, the usage of this type of controller does not provide an excellent response when the BDC operates outside of its operating point [21]. For instance, in [4], simulation results showed the DC–bus voltage instability when the DC–bus power suddenly changes. To overcome this issue, the authors of [22] have proposed an adaptive PI controller based on the Artificial Bee Colony Optimization algorithm. In [3], a robust integral sliding mode controller has been employed to control the BDC. Simulation results showed that the DC–link voltage response was improved compared to the PI controller. Still, the inductor current ripples are not attenuated.

Direct torque control (DTC) is commonly used to drive AC motors. The DTC with a two-level inverter uses a lookup table to select the appropriate switching vector (SV) from the eight available discrete vectors [5]. The SV is chosen so that the estimated torque and the stator flux amplitudes do not exceed hysteresis bands amplitudes. Recently, predictive torque control (PTC) has become a potential alternative to DTC [23]. In the traditional PTC, the discrete nonlinear model of the induction motor (IM) is used to predict the effect of the available SVs on the variables to be controlled. Afterwards, the optimal SV is selected by evaluating a cost function [13]. However, the real challenge for the PTC controller design is the choice of weighting factors. A poor choice of these factors can lead to significant torque ripples [24]. Besides, reducing those ripples requires a variable switching frequency. The limited number of SVs (SV_0–SV_7) in the two-level inverter (TLI) makes it unable to minimize torque ripples compared to multi-level inverters [25], except that this inverter is the most gainful in terms of cost and losses minimization. In the DTC and PTC methods the selected vector is applied during the entire control time T_{cont}, which increases the torque and flux ripples in the steady–state [26]. To decrease those ripples, the duty ratio control (DRC) approach is introduced in the literature. In the DRC, the selected SV is applied during a calculated period T_{ON}, and then a null vector (SV_0 or SV_7) is applied during the remainder of the control period (T_{cont}–T_{ON}) [27, 28].

The determination of the SV is also a crucial step for the design of the IM controller. A poor choice of this vector may not lead the controlled variables to their reference values. In [29], the PTC has been used to select the optimal SV by minimizing the predicted torque and flux errors. Still, the SV's choice is strongly dependent on the nonlinear model of the motor, which cannot guarantee an excellent operation under the parametric variation [26]. To solve this problem, the fuzzy controller is used in this contribution to determine precisely the suitable SV. The FLC is an intelligent structure that offers the designer the possibility of adjusting the controller's response according to his needs. The main advantage of this controller in this application is not sensitive to parametric variation like the PTC. Its design does not depend on the mathematical model of the induction motor [5]. Another advantage of the FLC is that it can significantly reduce initial torque ripples compared to DTC [28].

In the present work, hybrid fuzzy–predictive controllers are proposed to control a PV/battery water pumping system. The hybrid circuit shown in Fig. 1 has three stages. The first stage is a BDC which manages the exchange of energy between the DC-bus and the battery. The second stage is a boost converter (BC) which transmits the energy from the PV generator (PVG) to the DC-bus. The last stage is a TLI which feeds an IM. Each stage is controlled with a hybrid fuzzy–predictive controller. In the second stage, the FLC's role is to generate a variable SS reference current for the MPPT. This current is regulated with an MPC controller based on pulse width modulation (MPC–PWM). For controlling the BDC, an FLC is designed to provide the reference battery current that regulates the DC–bus voltage. Furthermore, two controllers based on PWM are designed to regulate the battery current. For controlling the IM, the DRC method is used. In the developed DRC controller, an FLC is designed to select the best active SV to be applied during T_{ON}. The selected SV achieves an initial regulation of the flux and the torque. The obtained SV is then used to create several virtual vectors (VV)s which have different activation times. These vectors will all be evaluated by a predictive algorithm, the best one which reduces the predicted torque error will be applied during the control period.

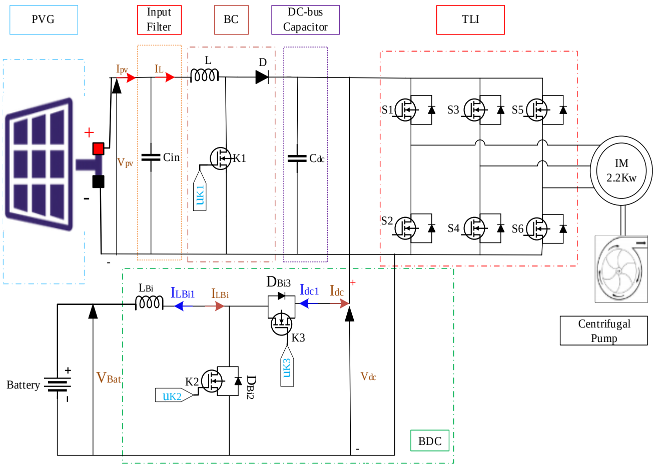

Fig. 1. The various stages of the PV/battery hybrid pumping system

2. Modelling of the Hybrid Pumping System

2.1. Modelling of the PV Array

A PV module is modelled by a photocurrent source in parallel with a diode (D_{module}) and a resistance (R_{shunt}). This model includes a resistance at the output terminal called series resistance (R_{series}). A single PV module is modelled using the following equation [30].

$$I_{mod} = I_{ph} - (V_{mod} + R_{series} I_{mod}) / R_{shunt} - I_r\left[\exp\left(q(V_{mod} + R_{series} I_{mod}) / (n_{series} aKT)\right) - 1\right] \quad (1)$$

Where I_{ph} is the photovoltaic current, I_r is the diode reverse leakage current, q is the charge of an electron, a is the ideality factor, K is Boltzman's constant, T is the temperature of the module, V_{mod} is the module output voltage, I_{mod} is the output current, n_{series} number of cells.

2.2. Modelling of the Boost Converter

The BC shown in Fig. 1 is commonly employed as the intermediate stage between the PV array and the DC–bus. This converter adjusts the PV voltage V_{pv} to track the MPP, and it increases the DC–link voltage V_{dc} according to the following formula [5].

$$V_{dc} = V_{pv} / (1 - D_{K1}) \quad (2)$$

Where, D_{K1} is the duty ratio. In the continuous conduction mode, Eq. (3) expresses the dynamic of the BC in terms of the state of switch K1 ($u_{K1} = 0$ if it is open and $u_{K1} = 1$ if the switch is closed) [3].

$$\begin{cases} \dot{V}_{dc} = (I_L - I_{dc}) / C_{dc} - (I_L / C_{dc}) u_{K1} \\ \dot{I}_L = (V_{pv} - V_{dc}) / L + (V_{dc} / L) u_{K1} \end{cases} \quad (3)$$

Where, C_{dc} and L are respectively the output capacitor and the inductance of the BC. V_{pv} and V_{dc} are respectively the input and the output voltages of the BC. I_{dc} is the DC-bus current, I_L is the inductor current.

2.3. Modelling of the Bidirectional Converter

The BDC shown in Fig. 1 is the most uncomplicated topology ensuring energy management between the high voltage side and the battery [20]. This converter operates in boost mode when the voltage V_{dc} needs to be increased. In this case, the average state space can be expressed similarly to Eq. (3).

$$\begin{cases} \dot{V}_{dc} = (I_{LBi} - I_{dc}) / C_{dc} - (I_{LBi} / C_{dc}) u_{K2} \\ \dot{I}_{LBi} = (V_{Bat} - V_{dc}) / L_{Bi} + (V_{dc} / L_{Bi}) u_{K2} \end{cases} \quad (4)$$

Where u_{K2} is the state of the switch K2, V_{Bat} is the battery voltage, I_{lBi} is the inductor current, L_{Bi} is the inductance of the BDC. The BDC also works in the buck mode to store the energy in the battery. In this scenario, the switch K2 stays inactive, and K3 is operational. The average state–space model for the buck mode is given by Eq. (5).

$$\begin{cases} \dot{V}_{dc} = (I_{dc1} / C_{dc}) - (I_{LBi1} / C_{dc}) u_{K3} \\ \dot{I}_{LBi1} = (-V_{Bat} / L_{Bi}) + (V_{dc} / L_{Bi}) u_{K3} \end{cases} \quad (5)$$

Where u_{K3} is the state of the switch K3, I_{lBi1} is the inductor current ($I_{lBi1} = -I_{lBi}$). I_{dc1} is the DC–bus current ($I_{dc1} = -I_{dc}$).

2.4. Modelling of the Asynchronous Motor

The best non–linear model that describes the IM's behavior is expressed in (α, β) reference frame. The matrix in Eq. (6) gives the relationship between the involved variables [29].

$$\begin{cases} \vec{\phi}_s = \vec{i}_s . L_s + \vec{i}_r . M \\ \vec{\phi}_r = \vec{i}_s . M + \vec{i}_r . L_r \\ \vec{v}_s = \vec{i}_s . R_s + (d\,\vec{\phi}_s / dt) \\ \vec{i}_r . R_r + (d\,\vec{\phi}_r / dt) - \underline{j} . \Omega_m . \vec{\phi}_r = \vec{0} \\ T_e = 1.5 p . \Im m\left(\vec{\phi}_s^{\,*} . \vec{i}_s\right) \\ J(d\Omega_m / dt) = T_e - T_p - f_r \Omega_m \end{cases} \quad (6)$$

Where $\vec{i}_s$, $\vec{i}_r$, $\vec{\phi}_s$, $\vec{\phi}_r$, and $\vec{v}_s$ are respectively: stator current vector, rotor current vector, stator flux vector, rotor flux vector, and stator voltage vector. T_p is the pump torque, T_e is the electrical torque, J is the inertia factor, p is the number of pole pairs, f_r is the friction coefficient, and Ω_m is the rotor speed. M, L_r, L_s are respectively the mutual, the rotor, and the stator inductances. R_r, R_s are the rotor and the stator resistances. $\underline{j}$ is the complex operator. Using Euler forward discretization and Eq. (6), the estimated stator and rotor fluxes are given by [26]:

$$\begin{cases} \vec{\phi}_s(j) = \vec{\phi}_s(j-1) + \tau_{pr} \vec{v}_s(j-1) - R_s \tau_{pr} \vec{i}_s(j-1) \\ \vec{\phi}_r(j) = (L_r / M) \vec{\phi}_s(j) + \left(M - (L_r L_s / M)\right) \vec{i}_s(j) \end{cases} \quad (7)$$

Where τ_{pr} is the time of prediction. The estimated electromagnetic torque at the instant j is expressed as,

$$T_e(j) = 1.5p \times \Im m\left(\vec{\phi}_s(j)^* \times \vec{i}_s(j)\right) \tag{8}$$

The stator flux angle is defined by:

$$\Psi_s = \arctan(\Im m(\vec{\phi}_s) / \Re e(\vec{\phi}_s)) \tag{9}$$

The predicted variables for current, stator flux, and electromagnetic torque are given in Eq. (10).

$$\begin{cases} \vec{\phi}_s(j+1) = \vec{\phi}_s(j) + \tau_{pr}\,(\vec{SV}(j) - R_s\,\vec{i}_s(j)) \\ \vec{i}_s(j+1) = \left(1 - (\tau_{pr} / T_\sigma)\right)\vec{i}_s(j) + \\ (\tau_{pr} / T_\sigma)\left[(\vec{\hat{\phi}}_r(j) / R_\sigma)\left(\left((T_r / \tau_r) - \underline{j}.T_r\Omega_m\right)\right) + \overrightarrow{SV}(j)\right] \\ T_e(j+1) = 1.5p \times \Im m\left(\vec{\phi}_s(j+1)^* \times \vec{i}_s(j+1)\right) \end{cases} \tag{10}$$

Where, $\overrightarrow{SV}$ is the active switching vector. $\tau_r=L_r/R_r$, $T_r=M/L_r$, $\sigma=1-(M^2/L_sL_r)$, $R_\sigma=R_s+T_r^2.R_r$, and $T_\sigma=\sigma L_s/R_\sigma$.

2.5. *Modelling of the pump*

A centrifugal pump is a suitable choice for pumping applications. It is the best choice for a high flow rate, and it produces water even at the lowest values of irradiance. According to Eq. (11), the centrifugal pump develops a resistive torque T_p proportional to the square of the speed.

$$T_p = K_{pump}\Omega_m^2 \tag{11}$$

Where K_{pump} is the pump proportionality constant [11].

3. Control Strategies

3.1. *Maximum Power Point Tracking*

3.1.1. *Presentation of the Conventional Current-based Perturb and Observe Algorithm*

The use of a current perturbation in MPPT methods is preferred under rapidly changing climatic conditions. It provides fast monitoring of the MPP thanks to the proportionality between the irradiance and the photovoltaic current [11]. The current-based P&O algorithm is shown in Fig. 2. First, this algorithm measures the photovoltaic current Ipv and the photovoltaic voltage V_{pv}, then the differential values of power ($\Delta P_{pv}=P_{pv}(j)-P_{pv}(j-1)$) and current ($\Delta Ipv=I_{pv}(j)-I_{pv}(j-1)$) are calculated. Secondly, the signs of the variables ΔI_{pv} and ΔP_{pv} are studied to know the position of the operating point with respect to the MPP. The signs help to determine whether the PV current should be perturbed positively or negatively. If a positive perturbation increases the PV power, the forward perturbation is maintained until the MPP is reached. In contrast, if a positive perturbation leads to power reduction, a backward perturbation is needed. Finally, this algorithm produces at the output a fixed step-size noted: $\pm\Delta I_{step}$, The produced reference current ($I_{pv(ref)}$) will serve as the input reference current for the boost converter.

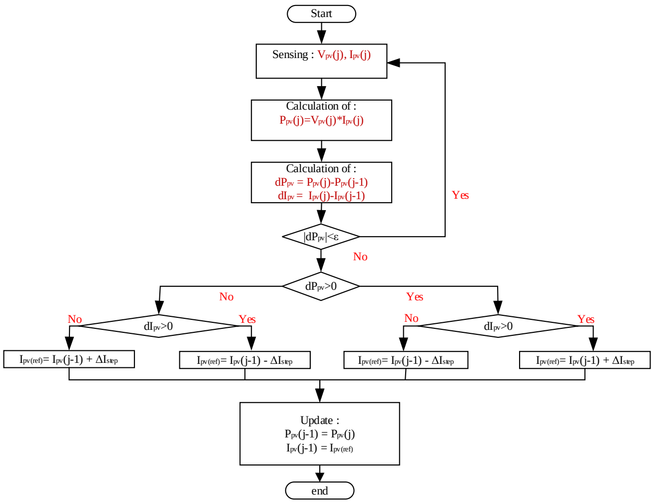

Fig. 2. Current-based P&O algorithm

3.1.2. *Presentation of the Proposed MPPT Algorithm*

The major drawback of the P&O algorithm is the slow dynamic of tracking during the sharp change of insolation, especially when a small current perturbation is selected. On the other side, a large current perturbation causes enormous power losses due to the continuous power fluctuation [11]. In this work, a Mamdani type FLC [8, 10, 31] will be employed to estimate the optimal SS, as shown in Fig. **3**. Such a method autotune the SS according to the position of the operating point.

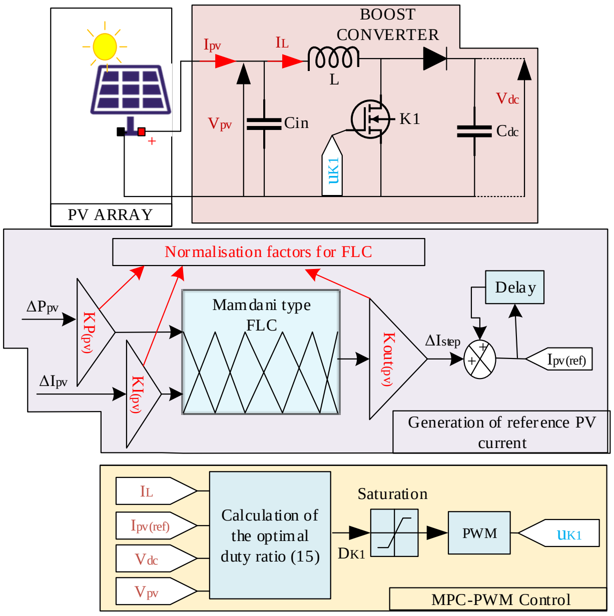

Fig. 3. The MPPT control scheme

When an abrupt variation of insolation occurs, the FLC generates a large perturbation to accelerate the tracking process. On the other hand, the FLC will enhance both the stability and the efficiency of tracking by selecting a small perturbation when the operating point is near the MPP. This fuzzy estimator considers the differential PV current ΔI_{pv} and the differential power ΔP_{pv} as inputs. The signs of the inputs help to determine whether a positive ($\Delta I_{step}>0$) or negative ($\Delta I_{step}<0$) SS will be applied, as given on the traditional P&O flowchart [13]. The values of these inputs determine how far the operating point is from the MPP. The membership functions are designed according to signs and the values of input variables, as illustrated in Fig. 4. +, ++ and +++ signs indicate the degree of positivity of the fuzzy variables. The signs -, -- and --- indicate the degree of negativity of the fuzzy variables.

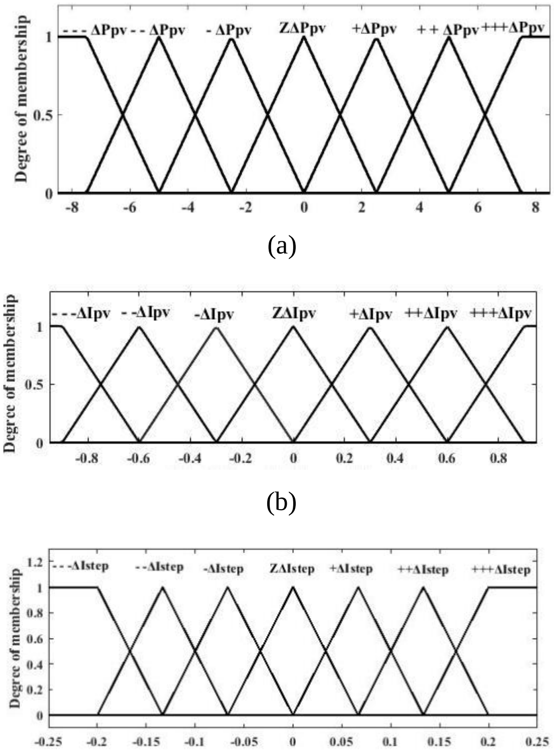

(a)

(b)

(c)

Fig. 4. Membership functions, (a) input ΔP_{pv}, (b) input ΔI_{pv}, (c) output ΔI_{step}

For the generation of the variable SS, the fuzzy rules presented in the Appendix (Table 1) are designed in such a way as to guarantee the best dynamic of tracking.

3.1.3. Control of the Input Current with MPC–PWM

The classical MPC applied to control the current I_{pv} evaluates a cost function defined by Eq. (12), then the best state of the switch K1 ($u_{K1}=0$ or $u_{K1}=1$) that minimizes this function is selected [13]. In that event, the switch may be triggered in each sampling time. That produces a variable switching frequency leading to excessive switching losses. Besides, the classical MPC might be the origin of huge current ripples [16]. The current ripples are not recommended for power converters since they increase power losses, especially when the inductor is connected to a non–linear source such as a photovoltaic generator [32]. For this reason, a model predictive control based on the PWM technique is used to overcome the traditional MPC limitations. In this technique, the current error is expressed with a second tracking error (Eq. (13)), which helps find the optimal duty cycle. Moreover, according to [16], minimizing this error helps to reduce the current ripples in steady–state conditions. Figure. 3 shows the control diagram of the MPC-PWM method.

$$I_{1error} = \left| I_{pv(ref)} - I_L(j) \right| \tag{12}$$

$$I_{1error} = T_{1ON}\left(dI_{LBi}/dt\right)_{u_{K1}=1} + T_{1OFF}\left(dI_{LBi}/dt\right)_{u_{K1}=0} \tag{13}$$

Where the terms $(dI_{LBi}/dt)u_{K1}=1$ and $(dI_{LBi}/dt)u_{K1}=0$ indicate the variation of the current through the inductor during T_{1ON} and T_{1OFF}, respectively. $T_1=T_{1ON}+T_{1OFF}$ is the full period of the PWM.

Replacing the state space equation (Eq. (3)) in Eq. (13), the current error becomes:

$$I_{1error} = (T_{1ON} - T_1)(V_{dc}(j)/L) + T_1(V_{pv}(j)/L) \tag{14}$$

Substituting the current error (Eq. (14)) in its original expression (Eq. (12)), the duty ratio can be obtained as,

$$D_{K1}(j) = (1/V_{dc}(j))\begin{pmatrix} (I_{pv(ref)} - I_L(j))(L/T_l) \\ +V_{dc}(j) - V_{pv}(j) \end{pmatrix} \tag{15}$$

3.2. Control of the Bidirectional Converter

The BDC shown in Fig. **5** operates in two independent modes. While switch K3 is active (switch K2 is inactive), the BDC works in the buck mode, and the energy is transmitted from the DC-bus side to the storage unit. On the contrary, while switch K2 is active (K3 is inactive), the battery is discharged to compensate for the energy gap in the DC–bus [3, 20].

High current ripples are a real problem that decreases battery life [33]. The common ways to make the current ripples lower are: choosing a large value of the inductance or selecting a high switching frequency. The above solutions increase the inductor size, and the switching losses become higher. Thanks to the advancement of power electronics circuits, various topologies were proposed to minimize current ripples' amplitude. For instance, a three-phase interleaved bidirectional converter is investigated in [34], which aims to reduce current ripples from 32.5% to 8%. In this paper, the classical bidirectional buck-boost converter is adopted to maintain the DC-bus voltage at the desired range. The BDC converter has many advantages, such as better efficiency, lucidity in design, and fewer components compared to other topologies. The classical MPC controller cannot minimize the amplitude of current ripples, as mentioned previously. Therefore, the MPC based on PWM is applied to the BDC to suppress the undesirable peak of current.

Fig. 5 shows the proposed controller that regulates the DC–bus voltage. In the proposed controller, a Takagi–Sugeno type FLC estimates the battery current required to keep the DC–bus voltage close to its nominal value. Then, an inner loop regulates the battery current with the MPC based on PWM.

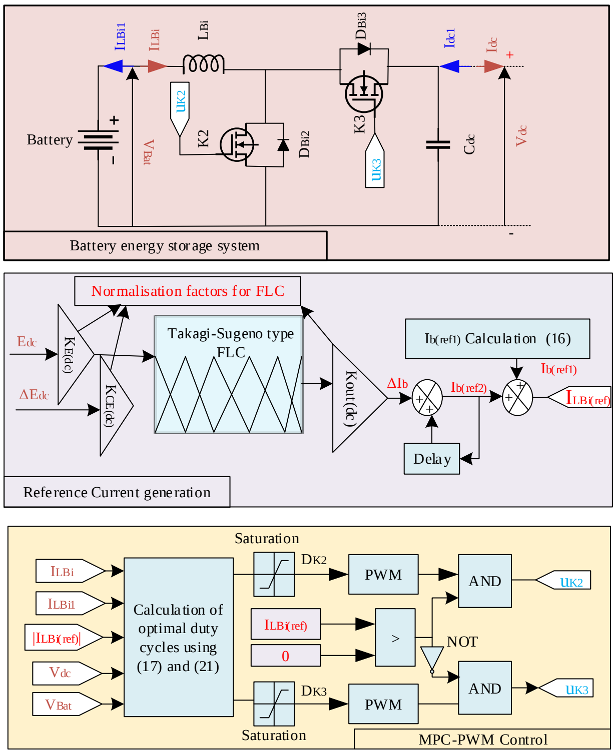

Fig. 5. Fuzzy–predictive controller for DC–bus voltage regulation

3.2.1. Generation of the Reference Current

In the absence of losses, the current delivered or absorbed by the battery can be calculated with the following equation:

$$I_{b(ref1)} = (T_e.\Omega_m - V_{pv}.I_{pv})/V_{Bat} \tag{16}$$

Fig. 5 shows that this equation (Eq. 16) gives an approximate value of the reference current. But it does not guarantee a perfect approximation due to the continuous variation of the system's total efficiency. Therefore, a Takagi-Sugeno (T-S) type FLC is chosen to adjust the value of the reference current. The T-S method is practical to work as an adaptive controller [35], so it is very suitable to manage the DC-bus power. The proposed FLC analyzes the sign of the voltage error ($E_{dc}(j)=V_{dc(ref)}-V_{dc}(j)$). If the error is positive, the FLC provides a positive step–size ($\Delta I_b>0$) to inject the current in the DC-bus. On the contrary, the FLC generates a negative reference current ($\Delta I_b<0$) to drive the current from the high-voltage side to the battery. The change of error ($\Delta E_{dc}(j) = E_{dc}(j) - E_{dc}(j-1)$) gives further information on the response of the system. It allows adjusting the amplitude of the step–size ΔI_b. Consequently, the dynamic of tracking will be improved in all conditions. Fig. 6 shows the membership functions of the input variables, and it shows that there are seven constant membership functions for the incremented step-size.

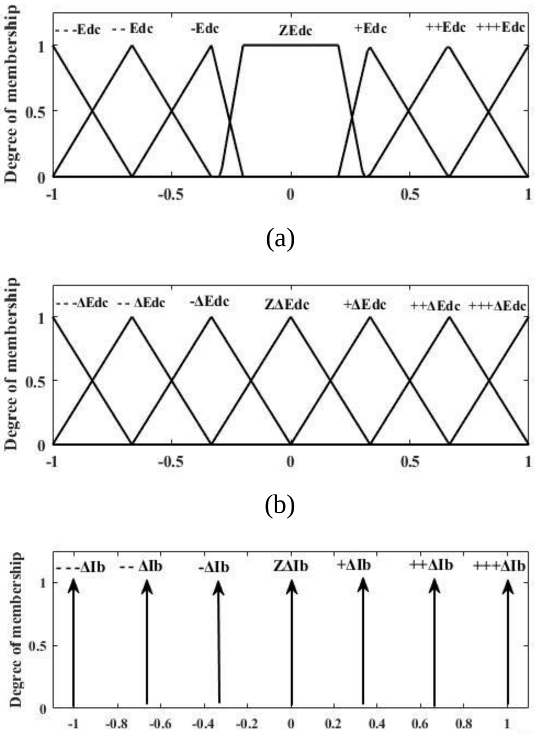

(a)

(b)

(c)

Fig. 6. Membership functions, (a) input E_{dc}, (b) input ΔE_{dc}, (c) output ΔI_b

For the DC–bus voltage regulation, the fuzzy rules presented in the Appendix (Table 2) are designed in such a way as to get the best steady-state performances.

3.2.2. Regulation of the Battery Current with MPC–PWM

The MPC–PWM method is proposed in this work to control the inductor current during the discharging mode. The same procedure as in the previous section can be used to synthesize the duty ratio D_{K2}.

$$D_{K2}(j) = (1/V_{dc}(j))\left[\begin{array}{l}(|I_{LBi(ref)}| - I_{LBi}(j))(L_{Bi}/T_2) \\ +V_{dc}(j) - V_{Bat}(j)\end{array}\right] \tag{17}$$

Where T_2 is the period of the PWM, $I_{LBi(ref)}$ is the reference current.

Similarly, the MPC-PWM can be applied to the buck converter during the charging phase. By analogy to Eq. (12), the original tracking error for the buck converter mode is defined by:

$$I_{3error} = \| I_{LBi(ref)} | - I_{LBi1}(j) | \tag{18}$$

Similar to the boost converter mode, the tracking error can be expressed in terms of the current slopes as,

$$I_{3error} = T_{3ON}\left(dI_{LBi1}/dt\right)_{u_{K3}=1} + T_{3OFF}\left(dI_{LBi1}/dt\right)_{u_{K3}=0} \tag{19}$$

Where $(dI_{LBi1}/dt)u_{K3}=1$ and $(dI_{LBi1}/dt)u_{K3}=0$ are the variation of the current through the inductor during T_{3ON} and T_{3OFF}, respectively. $T_3=T_{3ON}+T_{3OFF}$ is the full period of the PWM.

Substituting with the dynamic of the buck converter (Eq. (5)), the Eq. (19) could be rewritten as,

$$I_{3error} = (V_{dc}(j)/L_{Bi})T_{3ON} - (V_{Bat}(j)/L_{Bi})T_3 \tag{20}$$

Replacing the current error in its original form (Eq. (18)), the optimal duty ratio is given by.

$$D_{K3}(j) = (1/V_{dc}(j))\begin{bmatrix} (\left|I_{LBi(ref)}\right| \\ -I_{LBi1}(j))(L_{Bi}/T_3) + V_{Bat}(j) \end{bmatrix} \tag{21}$$

3.3. Duty Ratio Control of the Asynchronous Motor

3.3.1. Switching Vector Selection

For the duty ratio control technique, the SV is often selected from the DTC lookup table. The chosen SV is applied at the start of the control period to ensure an initial minimization of torque ripples [26]. To further improve the engine performances, a Mamdani-type FLC is used as an alternative to the conventional DTC. The designed FLC reduces both initial torque and flux ripples and improves the performances under transient conditions. Fig. 7(a), Fig. 7(b) and Fig. 7(c) show that the stator flux angle, the flux error ($E_\varphi = |\vec{\varphi}_{s(ref)}| - |\vec{\varphi}_s|$) and the torque error ($E_T = T_{e(ref)} - T_e$) are three variables involved in the fuzzification process. Triangular and trapezoidal membership functions are chosen to represent these variables due to their simplicity for implementation. The stator flux angle Ψ_s is represented with six triangular MFs, each MF defines a particular sector in the TLI vector diagram. Fig. 7(d) shows that there are eight possible switching vectors for the TLI, which are represented by singleton MFs. The Mean of Maximum technique (MOM) is employed for defuzzification [5, 28], where the crisp output is an SV_n (n=0...7) which has the maximum membership value.

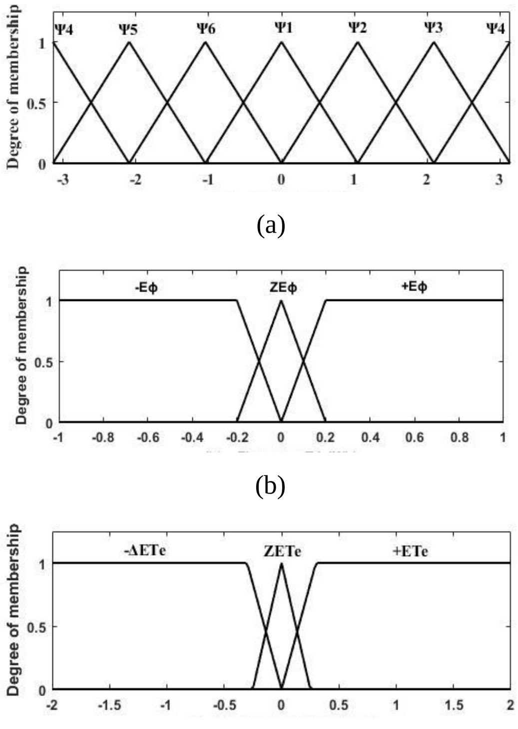

(a)

(b)

(c)

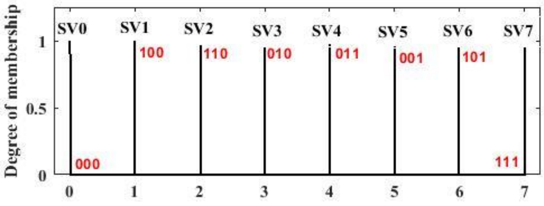

(d)

Fig. 7. Membership functions, (a) input Ψ_s, (b) input E_φ, (c) input E_{Te}, (d) switching action

For the generation of the SV, the fuzzy rules presented in the Appendix (

Table **3**) are designed in such a way as to reduce the flux ripples effectively and to achieve an initial tuning of the torque.

3.3.2. Calculation of T_{ON}

In the classical DTC, the SV is chosen from the DTC table [5]. The selected vector should be applied during a full period T_{cont}; this may increase or decrease the torque abruptly. To suppress the undesirable ripples, the SV vector should be applied during a precalculated period T_{ON}, and a zero vector is injected along the rest of the period ($T_{OFF}=T_{cont}-T_{ON}$). The zero vector causes a slight decrease of the electromagnetic torque [26]. Fig. 8 illustrates the DRC working principle.

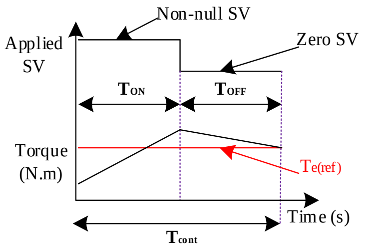

Fig. 8. The DRC working principle

The limited number of SVs in the TLI does not guarantee a perfect reduction of the torque ripples. To further minimize the torque ripples, the virtualization concept could be used by creating virtual vectors (VV)s. Fig. 9 shows that the VVs are synthesized from an SV given by the FLC stage. These vectors have the same direction but different lengths. Each VV_k can be defined by [26].

$$\overrightarrow{VV}_k = (1/m)\overrightarrow{SV} + ((m-j)/m)\overrightarrow{SV}_{Null} \;; \quad k \in [1, m] \tag{22}$$

Where m is the number of candidate virtual vectors. If the parameter m increases, the number of created vectors becomes large, and hence the magnitude of the torque ripples will be reduced. After defining the virtual vectors, the VV_k vector which minimizes the cost function (Eq. (23)), will be applied during the active switching period.

$$J(j) = |T_{e(ref)} - T_e(j+1)| + I_{s(\lim)} \tag{23}$$

The term $I_{s(lim)}$ is employed to protect the motor against overcurrent [29]. It takes a zero value when the predicted current is less than the maximal supported current ($|I_s(j+1)| \leq I_{max}$), and it takes an infinite value when the predicted current exceeds the maximum value ($|I_s(j+1)| > I_{max}$).

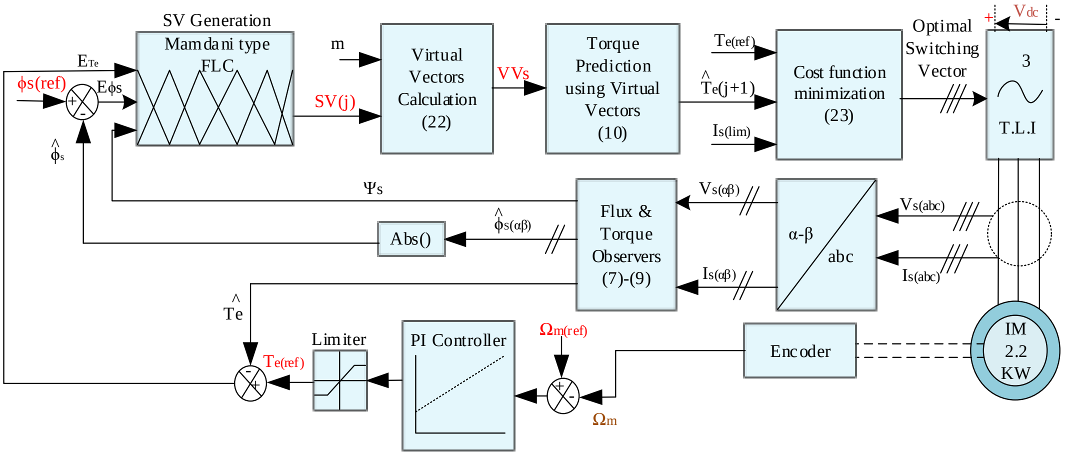

Fig. 9. DRC with a fuzzy–predictive controller

4. Simulation Results and Analysis

The suggested control scheme is assessed through a simulation employing MATLAB/Simulink software. The main parameters of the PVG and the IM are given in the Appendix (Table 4). Various profiles of irradiances and reference speeds are applied to the system, as shown in Fig. 10. Fig. 10(a) shows that the irradiance is decreased from 1000W/m² to 50W/m². Simultaneously, the reference speed is increased from 82.5rad/s to 143rad/s. Then, it is decreased to 128 rad/s, as shown in Fig. 10(b). The applied profiles allow the BESS to operate in all possible situations (Charging, discharging and Idle modes).

A comparison study is carried out within the same simulation conditions between the proposed control scheme and two control schemes presented in [3] and [4]. In [4], a perturb and observe algorithm based on the current perturbation is proposed for the MPPT. In this algorithm, a fuzzy inference system estimates the optimal value of the reference current $I_{pv(ref)}$, which corresponds to the MPP. The PV current is regulated with a simple sliding mode controller. Besides, two PI controllers were designed to control the BDC. Finally, the input–output linearization controller was used to drive the motor–pump. The authors of [3] have proposed a non–linear control scheme to ensure a robust operation of the hybrid pumping system. For the MPPT, a P&O algorithm provides the reference PV voltage, and a double integral sliding surface was designed to regulate this voltage. For the control of the DC–bus voltage, a controller based integral sliding surfaces was designed to control the BDC. The control of the engine was carried out by the non–linear predictive control. The third control scheme to be compared consists of the traditional perturb and observe algorithm for the MPPT [13]. The BDC is controlled with a fuzzy–predictive controller without the PWM control. Finally, the AC stage is controlled with the conventional predictive torque control [13].

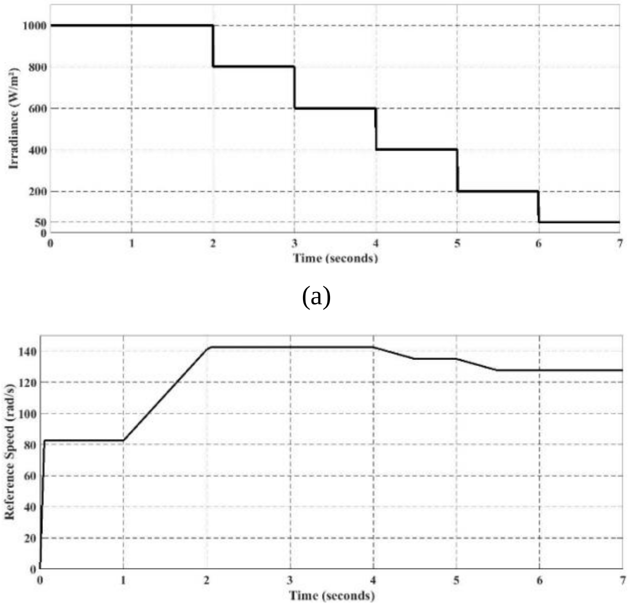

(a)

(b)

Fig. 10. Simulation inputs, (a) irradiance, (b) reference speed

Fig. 11(a) illustrates that the traditional P&O algorithm with a fixed step size of 0.025A has shown the lowest tracking performances in terms of the convergence speed and power stability in steady-state. When starting the system, the conventional algorithm fails to capture the MPP on the first try. The fixed step size makes the P&O unable to pursue the dynamic of the insolation change correctly. When the MPP is almost close, the P&O continues to generate the incremented reference current with the same amplitude, which lets the reference current go far from its optimal value, producing an undesirable drop of power at t=0.14s. The second compared MPPT algorithm is the P&O algorithm based on a fixed voltage perturbation of 0.01V. This algorithm tracks the MPP with the lowest speed compared to current–based perturbation algorithms. However, power fluctuations are significantly reduced with this algorithm, as shown in the different zoom views. Since the MPPT controller presented in this paper and the other one given in [4] use a fuzzy inference engine to generate a variable reference step–size, then the tracking dynamic is practically similar for both of them. The unique advantage of the developed MPPT controller is that the power oscillations are further reduced in steady-state as depicted in the zoom views. The MPPT algorithms based on the FLC offer the best tracking speed during the system's start-up. It can be observed from the first zoom view that the settling time is short (t=0.07s) with FLC–based MPPTs compared to P&O presented in [3] (t=0.7) and to the conventional P&O (t=0.5s). Fig. 11(b) shows the behavior of the inductor current I_L. The fuzzy–predictive controller based on the PWM presents the lowest current ripples, which positively influences the rate of ripples in the PV power curve. The SMC offers high stability, but the rate of current ripples is still high. The traditional P&O with a fixed SS has demonstrated high instability and huge current ripples in steady-state.

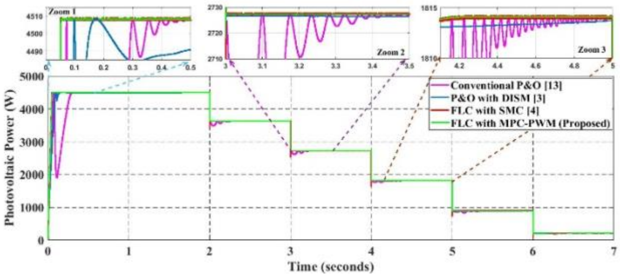

(a)

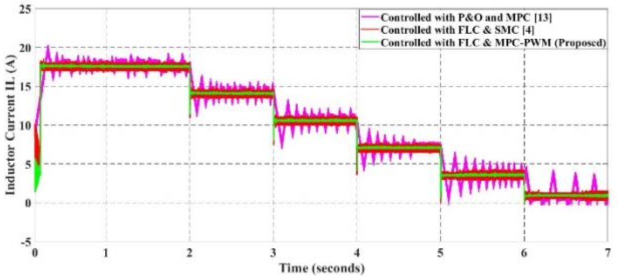

(b)

Fig. 11. The MPPT performances (a) PV power, (b) the inductor current I_L

Fig. 12(a) shows the behavior of the inductor current I_{LBi}. It can be seen that the developed controller minimizes the current ripples significantly by having a ripple range of 0.35A to 0.78A. The controller based on the fuzzy–predictive control without the PWM control shows larger current ripples by having a ripple range of 0.45A to 1.1A. On the other hand, the other controllers showed strong current ripples, which can reduce the reliability of the battery.

Initially, the DC–bus voltage is regulated with two PI controllers, as presented in [4]. It can be noticed from Fig. 12(b) that the measured voltage reaches its reference within a short settling time of 0.21s However, it presents an overshoot of 0.91%, the amplitude of voltage oscillations is large (4.2V peak–to–peak), and the steady–state error increases by up to 2.1V when the battery starts discharging. The DC-link voltage behavior is enhanced with the sliding mode controllers [3]. The overshoot is reduced to 0.55%, the peak–to–peak voltage amplitude is minimized to 1V, and the steady–state error is reduced to 0.5V. The proposed controller offers the best performances at the system start–up and in steady-state. The DC-link voltage reaches its reference smoothly with a null overshoot. In steady-state, the tracking error is practically null. The amplitude of voltage ripples is minimized to 0.47V peak–to–peak, which guarantees perfect stability and proper operation of the IM. Fig. 12(c) shows the battery state of charge (SOC) characteristic. The SOC increases when the BDC switches drive the current from the high-voltage side to the battery. Otherwise, the SOC decreases when the BDC injects the current into the DC-bus.

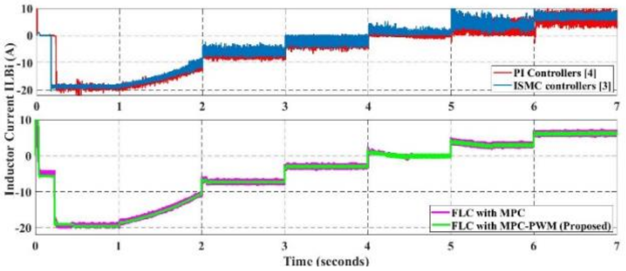

(a)

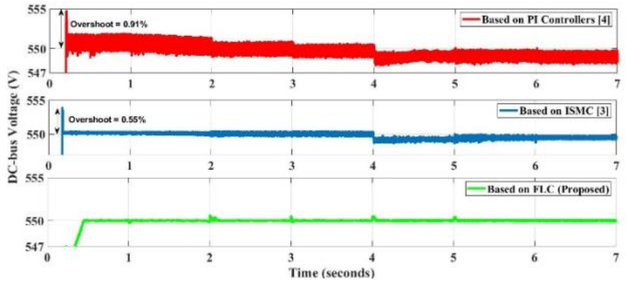

(b)

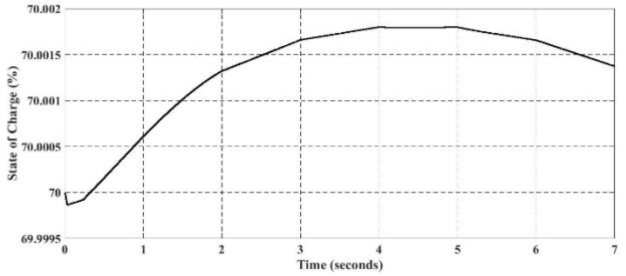

(c)

Fig. 12. The BESS performances (a) the inductor current I_{LBi}, (b) DC–link voltage, (c) the battery SOC

At the AC stage, the DRC is compared with three methods proposed in the literature, such as the conventional predictive torque control [13], the non–linear predictive control [3], and the input-output linearization control [4]. It can be seen from Fig. 13(a) that the controllers based on direct torque control offer the best torque dynamic and reduced ripples. This enhances the stability of the IM and the vibrations will be minimized. The proposed DRC is the best in terms of ripples reduction. It minimizes the ripples level up to ±0.24N.m. The PTC showed an acceptable range of ripples, which varies from ±0.5N.m to ±1.6N.m. In contrast, the other controllers have demonstrated high peaks of ripples. Furthermore, the PTC and the fuzzy–predictive controller can limit the intense increase of the torque during the engine's starting by limiting the reference torque with a saturation function. The torque is limited to 18N.m, which protects the motor from overcurrent and helps to start the motor smoothly.

Fig. 13(b) demonstrates that the methods based on direct torque control show the best accuracy of speed tracking and the lowest speed oscillations in steady-state. At the start–up, the non–linear controllers reach the reference speed (82.5rad/s) instantaneously due to the intense produced electromagnetic torque. The limitation of the reference torque at 18N.m for DTC methods delays the mechanical dynamics of the motor to reach the reference speed.

Fig. 13(c) shows the stator fluxes regulated by the PTC and the DRC. In the conventional PTC, the selected SV is applied to simultaneously reduce the errors of the torque and the stator flux. In the proposed controller, the FLC is designed to generate the optimal vector which minimizes the stator flux error and achieves initial torque regulation. Then, the predictive algorithm calculates the appropriate duty ratio which reduces the torque ripple. For these reasons, the steady-state flux error is improved with the proposed controller, and the ripples rate is reduced by up to 0.01Wb peak-to-peak. In contrast, the flux controlled with the PTC presents large ripples by having a ripple rate of 0.021Wb peak-to-peak.

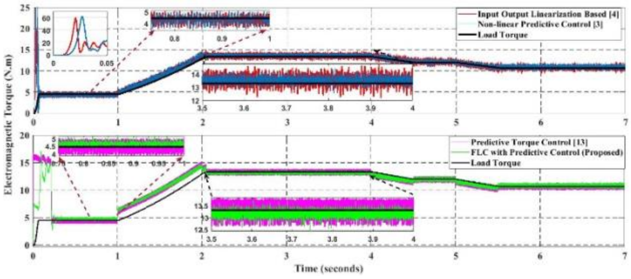

(a)

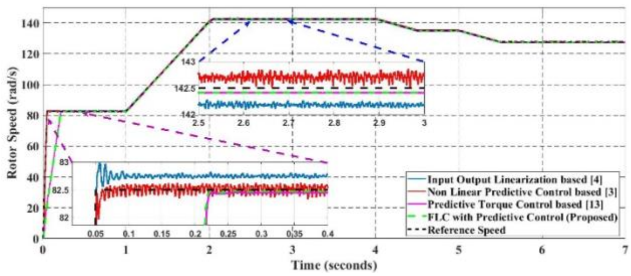

(b)

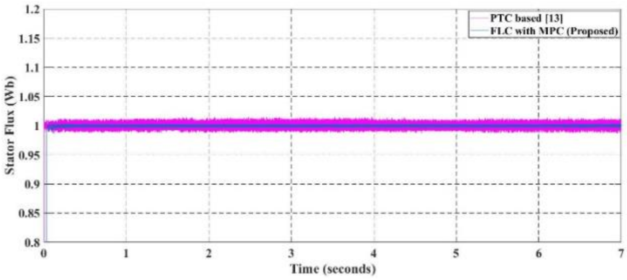

(c)

Fig. 13. The IM parameters (a) torque, (b) rotor speed, (c) stator flux

5. Conclusion

This contribution deals with the design of fuzzy–predictive controllers for a pumping system powered by a battery and a 4.5KW photovoltaic source, aiming to improve the PV power usage. The suggested controllers were compared with three control schemes proposed in the literature. Simulation results indicated the superiority of the suggested controllers at any stage of the system. They present the best performances in terms of:

(1) MPPT control: the proposed fuzzy-predictive MPPT controller showed the fastest tracking dynamic and the lowest fluctuations of the PV power.

(2) Current ripples reduction: the predictive controllers based on PWM have reduced the current ripples for the BC and the BDC.

(3) DC-bus voltage regulation: the fuzzy-predictive controller has demonstrated the minimum overshoot, a null steady-state error, and the voltage ripples were reduced up to 0.47V peak-to-peak.

(4) Torque and flux ripples minimization: the level of torque ripples was reduced up to ± 0.24N.m, and the flux ripples rate was reduced by up to 0.01Wb peak-to-peak.

$\boldsymbol{\Delta P_{pv}}$							
$\boldsymbol{\Delta I_{pv}}$	$---\Delta P_{pv}$	$--\Delta P_{pv}$	$-\Delta P_{pv}$	$Z\Delta P_{pv}$	$+\Delta P_{pv}$	$++\Delta P_{pv}$	$+++\Delta P_{pv}$
$---\Delta I_{pv}$	$+++\Delta I_{step}$	$+++\Delta I_{step}$	$++\Delta I_{step}$	$-\Delta I_{step}$	$--\Delta I_{step}$	$---\Delta I_{step}$	$---\Delta I_{step}$
$--\Delta I_{pv}$	$++\Delta I_{step}$	$++\Delta I_{step}$	$++\Delta I_{step}$	$-\Delta I_{step}$	$--\Delta I_{step}$	$--\Delta I_{step}$	$---\Delta I_{step}$
$-\Delta I_{pv}$	$++\Delta I_{step}$	$+\Delta I_{step}$	$+\Delta I_{step}$	$Z\Delta I_{step}$	$-\Delta I_{step}$	$-\Delta I_{step}$	$--\Delta I_{step}$
$Z\Delta I_{pv}$	$Z\Delta I_{step}$	$Z\Delta I_{step}$	$Z\Delta I_{step}$	$Z\Delta I_{step}$	$-\Delta I_{step}$	$-\Delta I_{step}$	$-\Delta I_{step}$
$+\Delta I_{pv}$	$--\Delta I_{step}$	$-\Delta I_{step}$	$-\Delta I_{step}$	$Z\Delta I_{step}$	$+\Delta I_{step}$	$+\Delta I_{step}$	$++\Delta I_{step}$
$++\Delta I_{pv}$	$--\Delta I_{step}$	$-\Delta I_{step}$	$-\Delta I_{step}$	$Z\Delta I_{step}$	$+\Delta I_{step}$	$+\Delta I_{step}$	$++\Delta I_{step}$
$+++\Delta I_{pv}$	$---\Delta I_{step}$	$--\Delta I_{step}$	$--\Delta I_{step}$	$Z\Delta I_{step}$	$++\Delta I_{step}$	$++\Delta I_{step}$	$+++\Delta I_{step}$

Appendix

Table 1. FLC rules for the generation of a variable SS

Table 2. FLC rules for the DC-bus voltage regulation

E_{dc}							
ΔE_{dc}	---E_{dc}	--E_{dc}	-E_{dc}	ZE_{dc}	+E_{dc}	++E_{dc}	+++E_{dc}
---ΔE_{dc}	---ΔI_b	--ΔI_b	-ΔI_b	-ΔI_b	--ΔI_b	-ΔI_b	ZΔI_b
--ΔE_{dc}	--ΔI_b	--ΔI_b	-ΔI_b	-ΔI_b	--ΔI_b	ZΔI_b	+ΔI_b
-ΔE_{dc}	--ΔI_b	-ΔI_b	-ΔI_b	ZΔI_b	ZΔI_b	+ΔI_b	++ΔI_b
ZΔE_{dc}	-ΔI_b	-ΔI_b	ZΔI_b	ZΔI_b	ZΔI_b	+ΔI_b	++ΔI_b
+ΔE_{dc}	-ΔI_b	-ΔI_b	ZΔI_b	ZΔI_b	+ΔI_b	++ΔI_b	++ΔI_b
++ΔE_{dc}	-ΔI_b	ZΔI_b	+ΔI_b	+ΔI_b	++ΔI_b	++ΔI_b	+++ΔI_b
+++ΔE_{dc}	ZΔI_b	+ΔI_b	+ΔI_b	+ΔI_b	++ΔI_b	+++ΔI_b	+++ΔI_b

Table 3 FLC rules for the generation of the SV

Ψ_s		Ψ_1	Ψ_2	Ψ_3	Ψ_4	Ψ_5	Ψ_6
E_φ	E_{Te}						
-E_φ	-E_{Te}	SV_5	SV_6	SV_1	SV_2	SV_3	SV_4
	ZE_{Te}	SV_0	SV_7	SV_0	SV_7	SV_0	SV_7
	+E_{Te}	SV_3	SV_4	SV_5	SV_6	SV_1	SV_2
ZE_φ	-E_{Te}	SV_0	SV_0	SV_0	SV_0	SV_0	SV_0
	ZE_{Te}	SV_0	SV_0	SV_0	SV_0	SV_0	SV_0
	+E_{Te}	SV_3	SV_4	SV_4	SV_5	SV_6	SV_2
+E_φ	-E_{Te}	SV_6	SV_1	SV_2	SV_3	SV_4	SV_5
	ZE_{Te}	SV_7	SV_0	SV_7	SV_0	SV_7	SV_0
	+E_{Te}	SV_2	SV_3	SV_4	SV_5	SV_6	SV_1

Table 4. The principal parameters of the hybrid pumping system

	Parameter	**Value**
PV generator	Optimal current (I_{mp}) at STC	17.68A
	Optimal voltage (V_{mp}) at STC	255V
	Optimal Power (P_{mp}) at STC	4508.4W
Induction Motor	Rated Power (P_r)	2200W
	Rated Speed (Ω_r)	150 rad/s
	Rated Frequency (f)	50Hz
	Rated Flux ($\phi_{s(ref)}$)	1Wb
	Reference DC-link voltage ($V_{dc(ref)}$)	550V
	Stator Resistance (R_s)	4.125Ω
	Rotor Resistance (R_r)	2.486Ω
	Stator Inductance (L_s)	0.3004H
	Rotor Inductance (L_r)	0.3004H
	Mutual Inductance (M)	0.2848H
	Number of pole pairs (p)	2
	Inertia (J)	0.031Kg.m²
	Viscous friction coefficient (f_r)	0.0058N.m/(rad/s)

References

[1] G. Chbirik, Z. Massaq, A. Abounada, and M. Mabrouki, “Speed Control of Induction Motor Driving a Pump Supplied by a Photovoltaic Array,” *International Journal of Renewable Energy Research (IJRER)*, vol. 10, no. 1, Art. no. 1, Mar. 2020.

[2] Z. Massaq, A. Abounada, O. Benkirane, and M. Ramzi, “Modern Control of a Standalone Solar Pumping System Based on Asynchronous Motor,” in *2021 9th International Renewable and Sustainable Energy Conference (IRSEC)*, Nov. 2021, pp. 1–6.

[3] Z. Massaq, A. Abounada, and M. Ramzi, “Robust non-linear control of a hybrid water pumping system based on induction motor,” *International Journal of Power Electronics and Drive Systems (IJPEDS)*, vol. 11, no. 4, Art. no. 4, Dec. 2020.

[4] Z. Massaq, A. Abounada, A. Brahmi, and M. Ramzi, “Control of PV-Battery Based Hybrid Water Pumping System Under Sudden Irradiance and Speed Changes,” in *2020 IEEE 6th International Conference on Optimization and Applications (ICOA)*, Apr. 2020.

[5] M. Errouha, A. Derouich, S. Motahhir, O. Zamzoum, N. El Ouanjli, and A. El Ghzizal, “Optimization and control of water pumping PV systems using fuzzy logic controller,” *Energy Reports*, vol. 5, pp. 853–865, Nov. 2019.

[6] Y.-T. Chen, Z.-H. Lai, and R.-H. Liang, “A novel auto-scaling variable step-size MPPT method for a PV system,” *Solar Energy*, vol. 102, pp. 247–256, Apr. 2014.

[7] O. Guenounou, A. Belkaid, I. Colak, B. Dahhou, and F. Chabour, “Optimization of Fuzzy Logic Controller Based Maximum Power Point Tracking Using Hierarchical Genetic Algorithms,” in *2021 9th International Conference on Smart Grid (icSmartGrid)*, Jun. 2021, pp. 207–211.

[8] K. Kayisli, R. Z. Caglayan, N. Zhakiyev, A. Harrouz, and I. Colak, “A Review of Hybrid Renewable Energy Systems and MPPT Methods,” *International Journal of Smart Grid - ijSmartGrid*, vol. 6, no. 3, Art. no. 3, Sep. 2022.

[9] M. Sarra, A. Belkaid, I. Colak, G. Boudechiche, and K. Kayisli, “Fuzzy-MPPT Controller Based Solar Shunt Active Power Filter,” in *2022 11th International Conference on Renewable Energy Research and Application (ICRERA)*, Sep. 2022, pp. 436–440.

[10] J. Macaulay and Z. Zhou, “A Fuzzy Logical-Based Variable Step Size P&O MPPT Algorithm for Photovoltaic System,” *Energies*, vol. 11, no. 6, Art. no. 6, Jun. 2018.

[11] Z. Massaq, G. Chbirik, A. Abounada, A. Brahmi, and M. Ramzi, “Control of Photovoltaic Water Pumping System Employing Non-Linear Predictive Control and Fuzzy Logic Control,” *International Review on Modelling and Simulations (IREMOS)*, vol. 13, no. 6, Art. no. 6, Dec. 2020.

[12] A. Cervone, L. P. Di Noia, R. Rizzo, I. Spina, and R. Miceli, “A Constrained Optimal Model Predictive Control for Mono Inverter Dual Parallel PMSM Drives,” in *2018 7th International Conference on Renewable Energy Research and Applications (ICRERA)*, Oct. 2018, pp. 1501–1507.

[13] B. Talbi, F. Krim, T. Rekioua, S. Mekhilef, A. Laib, and A. Belaout, “A high-performance control scheme for photovoltaic pumping system under sudden irradiance and load changes,” *Solar Energy*, vol. 159, pp. 353–368, Jan. 2018.

[14] F. Sebaaly, H. Vahedi, H. Y. Kanaan, and K. Al-Haddad, “Experimental Design of Fixed Switching Frequency Model Predictive Control for Sensorless Five-Level Packed U-Cell Inverter,” *IEEE Transactions on Industrial Electronics*, vol. 66, no. 5, pp. 3427–3434, May 2019.

[15] M. Aguirre, S. Kouro, C. A. Rojas, J. Rodriguez, and J. I. Leon, “Switching Frequency Regulation for FCS-MPC

Based on a Period Control Approach," *IEEE Transactions on Industrial Electronics*, vol. 65, no. 7, pp. 5764–5773, Jul. 2018.

[16] R. B. A. Cunha, R. S. Inomoto, J. A. T. Altuna, F. F. Costa, S. G. Di Santo, and A. J. Sguarezi Filho, "Constant switching frequency finite control set model predictive control applied to the boost converter of a photovoltaic system," *Solar Energy*, vol. 189, pp. 57–66, Sep. 2019.

[17] A. Sahbani, K. Cherif, and K. B. Saad, "Multiphase Interleaved Bidirectional DC-DC Converter for Electric Vehicles and Smart Grid Applications," *International Journal of Smart Grid - ijSmartGrid*, vol. 4, no. 2, Art. no. 2, Jun. 2020.

[18] V. F. Pires, A. Cordeiro, D. Foito, and J. F. Silva, "Control of Bidirectional Quadratic DC-DC Converters for Storage Support of DC Power Grids," in *2018 7th International Conference on Renewable Energy Research and Applications (ICRERA)*, Oct. 2018, pp. 227–232.

[19] Moubarak, G. El-Saady, and E.-N. A. Ibrahim, "Battery energy storage for variable speed photovoltaic water pumping system." engrXiv, Jan. 07, 2019.

[20] B. Y. Li, C. Xu, C. Li, and Z. Guan, "Working principle analysis and control algorithm for bidirectional DC/DC converter," p. 9, 2017.

[21] Etxeberria, I. Vechiu, H. Camblong, and J.-M. Vinassa, "Comparison of Sliding Mode and PI Control of a Hybrid Energy Storage System in a Microgrid Application," *Energy Procedia*, vol. 12, pp. 966–974, Jan. 2011.

[22] I. E. Atawi and A. M. Kassem, "Optimal Control Based on Maximum Power Point Tracking (MPPT) of an Autonomous Hybrid Photovoltaic/Storage System in Micro Grid Applications," *Energies*, vol. 10, no. 5, Art. no. 5, May 2017.

[23] N. El Ouanjli *et al.*, "Modern improvement techniques of direct torque control for induction motor drives - a review," *Protection and Control of Modern Power Systems*, vol. 4, no. 1, p. 11, May 2019.

[24] A. Ammar, B. Talbi, T. Ameid, Y. Azzoug, and A. Kerrache, "Predictive direct torque control with reduced ripples for induction motor drive based on T-S fuzzy speed controller," *Asian Journal of Control*, vol. 21, no. 4, pp. 2155–2166, 2019.

[25] N. El Ouanjli *et al.*, "Direct torque control of doubly fed induction motor using three-level NPC inverter," *Protection and Control of Modern Power Systems*, vol. 4, no. 1, p. 17, Oct. 2019.

[26] M. R. Nikzad, B. Asaei, and S. O. Ahmadi, "Discrete Duty-Cycle-Control Method for Direct Torque Control of Induction Motor Drives With Model Predictive Solution," *IEEE Transactions on Power Electronics*, vol. 33, no. 3, pp. 2317–2329, Mar. 2018.

[27] M. R. Nikzad, "An improved single-vector-based Duty Cycle Control Method for Direct Torque Control of Induction Motor," in *2020 11th Power Electronics, Drive Systems, and Technologies Conference (PEDSTC)*, Feb. 2020, pp. 1–5.

[28] S. H., K. S.f., and S. B., "Improvements in direct torque control of induction motor for wide range of speed operation using fuzzy logic," *Journal of Electrical Systems and Information Technology*, vol. 5, no. 3, pp. 813–828, Dec. 2018.

[29] A. Ammar, B. Talbi, T. Ameid, Y. Azzoug, and A. Kerrache, "Predictive direct torque control with reduced ripples for induction motor drive based on T-S fuzzy speed controller," *Asian Journal of Control*, vol. 21, no. 4, pp. 2155–2166, 2019.

[30] Vinod, R. Kumar, and S. K. Singh, "Solar photovoltaic modeling and simulation: As a renewable energy solution," *Energy Reports*, vol. 4, pp. 701–712, Nov. 2018.

[31] B. A. Naidu and S. A. Kumar, "Fuzzy Intelligent Controller for the MPPT of a Photovoltaic Module in comparison with Perturb and Observe algorithm," vol. 13, no. 11, p. 5, 2018.

[32] H. E. Khateb, N. A. Rahim, J. Selvaraj, and B. W. Williams, "DC-to-DC Converter with Low Input Current Ripple for Maximum Photovoltaic Power Extraction," *IEEE Transactions on Industrial Electronics*, vol. 62, no. 4, pp. 2246–2256, Apr. 2015.

[33] K. Uddin, A. D. Moore, A. Barai, and J. Marco, "The effects of high frequency current ripple on electric vehicle battery performance," *Applied Energy*, vol. 178, pp. 142–154, Sep. 2016.

[34] W. Lee, B. Han, and H. Cha, "Battery ripple current reduction in a three-phase interleaved dc-dc converter for 5kW battery charger," in *2011 IEEE Energy Conversion Congress and Exposition*, Sep. 2011, pp. 3535–3540.

[35] F. Cavallaro, "A Takagi-Sugeno Fuzzy Inference System for Developing a Sustainability Index of Biomass," *Sustainability*, vol. 7, no. 9, pp. 12359–12371,Sep.2015.